To the Graduate Council:

I am submitting herewith a thesis written by Ivan G. Dors entitled "Experimental Investigations of Aluminum Monoxide in the Laser Ablation of Alumina." I have examined the final copy of this thesis for form and content and recommend that it be accepted in partial fulfillment of the requirements for the degree of Masters of Science, with a major in Physics.

Christian Parigger

Dr. C. G. Parigger, Major Professor

We have read this thesis
and recommend its acceptance:

Dr. J. W. L. Lewis

Lloyd M Davis

Dr. L. M. Davis

Accepted for the Council:

Associate Vice Chancellor and
Dean of The Graduate School

EXPERIMENTAL INVESTIGATIONS OF ALUMINUM MONOXIDE IN THE LASER ABLATION OF ALUMINA

A Thesis

Presented for the

Master of Science

Degree

The University of Tennessee, Knoxville

Ivan George Dors

May 1998

Dedication

This thesis is dedicated to my parents

Mr. Thomas E. Dors

and

Mrs. Claire L. Dors

and to my brother

Mr. Eric E. Dors

who have given me invaluable support

in all my endeavors.

Acknowledgements

I would like to thank the people who have contributed to this work. To start, I would like to thank Dr. C. G. Parigger and Dr. J. W. L. Lewis for their support, guidance, and enthusiasm. In addition, I would like to show appreciation to my committee of Dr. C. G. Parigger, Dr. J. W. L. Lewis, and Dr. L. M. Davis for the meticulous corrections to get the thesis into its final form. Thanks to J. O. Hornkohl for support with the computation and analysis of diatomic molecular spectra, and N. Wright for technical assistance. I would finally like to acknowledge C. Rathje and Y. Li for initial investigations and work on the creation of the AlO line strength file. This material is based upon work that is in part supported by the National Science Foundation under Grant No. CTS-9512489 and a UTSI graduate research assistantship.

Abstract

The laser ablation of alumina (Al_2O_3) is experimentally investigated by the use of ultra high speed photography, scanning electron microscopy, quadrupole mass spectroscopy, and time-resolved optical spectroscopy. Irradiance levels of typically 5 GW/cm^2 frequency quadrupled Nd:YAG laser radiation are applied to achieve uv laser ablation. Of primary interest is the optical spectroscopy of the aluminum monoxide (AlO) blue-green $B^2\Sigma^+ \longrightarrow X^2\Sigma^+$ band system that dominates the emission spectra some 20 μs after the short pulse, high peak power laser surface interaction. Comparisons with synthetic spectra that are computed by the use of accurate diatomic line strengths indicate AlO temperatures well in excess of 3,000 K. Monte-Carlo simulations are implemented to estimate the precision of the temperature obtained from (1) least-square fitting the entire measured spectrum, and (2) applying Boltzmann plot methods and Savitzky-Golay numerical filters to extract spectral peaks. The spectroscopic temperature obtained from both approaches (1) and (2) are typically within two standard deviations and show a precision on the order of 1%.

Contents

List of Figures

List of Tables

1 Introduction

High temperature spectra are of interest in the study of the anharmonic effects in the AlO B state on the molecular line strength calculation, in the characterization of various plasma phenomena and in diagnostics applications to describe gas-dynamic plume effects. In this work, an investigation is presented of such spectra and the plume dynamics created by the laser ablation of alumina.

1.1 Aluminum Monoxide

The spectrum of aluminum monoxide (AlO) has been thoroughly investigated in the past due to its presence in several scientific fields. In astrophysics, AlO absorption bands have been measured in sun spots and stellar emission bands have been observed from the M-type star 'o Ceti' [1]. In the area of space exploration, AlO is important due to its problematic presence in re-entry wakes and solid-fuel rocket exhaust [2]. Additionally, AlO spectral measurements of high-altitude TNT explosions have allowed approximate temperature measurements of the upper atmosphere [3].

In the past, laboratory experiments have been performed to measure the spectrum of AlO. For these experiments there have been various methods implemented to produce AlO in the excited $B^2\Sigma^+$ state. Among these experiments are included flame emission [2], shock tube [4], vacuum discharge tube [5], hollow cathode [6], N_2O reaction with Al vapor [7], and the laser ablation of Al_2O_3 [8, 9, 10]. These methods produced AlO with temperatures ranging from 360 K to 4,750 K in ambient pressures ranging from 10^{-8} to 1 atmosphere. The resolution of these recorded spectra

range from those with resolved rotational bands to those with unresolved vibrational bands. In the following work, the AlO spectra are emitted during short-pulse, high peak power laser ablation of alumina. All spectroscopic measurements are performed in 1 atmosphere of laboratory air, unless noted otherwise.

The primary interest of this work is the study of high temperature AlO spectra that is produced in the plasma of laser-ablated Al_2O_3. The specific objective of the research is to measure the temperature of the recombination AlO in the expansion plasma using the spontaneous emission spectra of the AlO $B^2\Sigma^+ \longrightarrow X^2\Sigma^+$ electronic transition. To accomplish this objective, optical spectroscopic data are experimentally measured and, with synthetic spectra predicted by molecular line strengths, the temperature (T) of an assumed local thermal equilibrium (LTE) sample is obtained. The Nelder-Mead and Diatomic Boltzmann plot techniques (NMT and DBP, respectively) are used to find T, and quantification of the goodness-of-fit of the results is an essential element of this objective.

1.2 The Ablation Process

In the laser ablation process, an incident laser pulse of sufficient intensity ionizes target molecules and a plasma is formed. With a nanosecond-duration pulse, once the plasma is created, it absorbs the remaining energy of the pulse and acts as a buffering interface between the pulse and the target. Figure 1 illustrates the breakdown characteristics of a typical nanosecond laser pulse [11]. The breakdown threshold, which is defined as the irradiance level for which the probability of breakdown is 50%, is

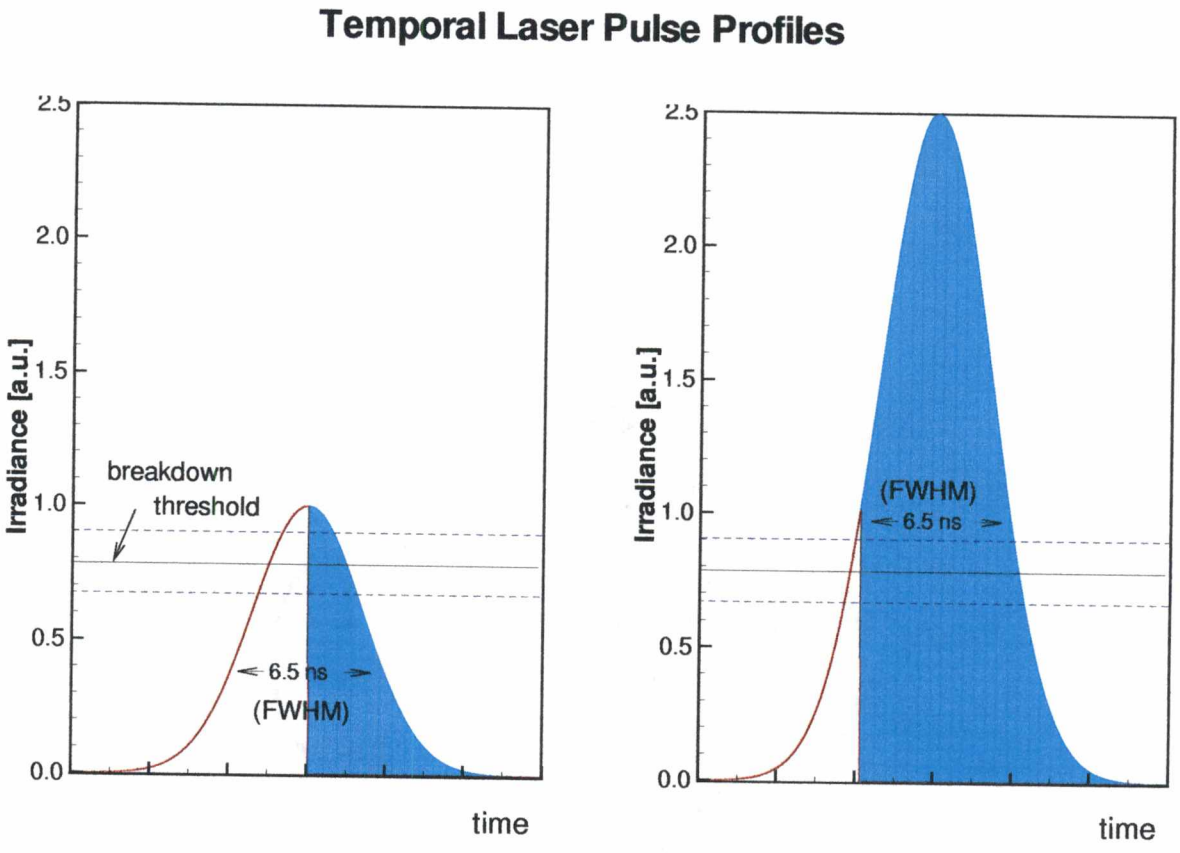

Figure 1: Temporal laser pulse profiles and the breakdown threshold.

shown as a solid horizontal line. The two broken horizontal lines show the irradiance levels for which the probability of breakdown is 33% and 67%. The profile on the left shows a laser pulse with the minimal peak irradiance required to induce breakdown of a given substance. The right profile shows a pulse with peak irradiance 2.5 times larger than the breakdown threshold. In both profiles, the area of the unshaded region indicates the mean fluence required for breakdown, while that of the shaded region is the amount of energy that pumps the plasma. For femtosecond laser pulses, it is possible for the rate of energy transfer to the surface of the target to be faster than the reaction time of the material. This allows the ability to put more energy into a target (compared with that of a nanosecond pulse) due to the lack of plasma shielding of the surface.

In recent years the process of laser ablation has become one of importance. It has been applied to numerous operations such as fabrication of thin films, micromachining, surface treatment, and welding. The laser ablation of alumina (Al_2O_3) has been found to produce AlO in the excited $B^2\Sigma^+$ state. In previous investigations [8, 9, 10, 12, 13], nominal nanosecond excimer lasers were preferred to induce the ablation process. Recently, applications of nominal picosecond and femtosecond radiation have been reported [14]. Ultraviolet radiation is capable of driving the process. A frequency quadrupled neodymium-yttrium-aluminum-garnet laser (Nd:YAG) is used in the following work. Typically, 5 mJ per 6.5 ns pulse is sufficient for 266 nm laser ablation of alumina. Note that the wavelength of the uv laser radiation is outside the spectral region of our interest.

2 The Laser System

In this section, a detailed description of the general experimental arrangement shown in Figure 2, will be reported. Specifically, the optical and timing setup for the laser ablation of alumina will be explained.

2.1 Optical Arrangement

A Nd:YAG Q-switched laser system (Continuum Model YG680S-10) was used for ablating an alumina target. This laser system has a type II KD*P crystal to generate laser light at the second harmonic (532 nm) of the Nd:YAG nominal 1064 nm radiation wavelength. Since the effects of the fourth harmonic (266 nm) were of primary interest, an Inrad Autotracker II external frequency doubler was integrated into the system. The optical setup was arranged such that the 532 nm radiation produced by the laser was reflected by two mirrors, and was incident on the external frequency doubler. Although the Inrad Autotracker II is easily adjusted for optimized frequency doubling, the product beam of the external frequency doubler was not pure 266 nm radiation. One dichoric mirror was used to filter out the majority of the 532 nm radiation, so that the target positioned in the vacuum chamber was primarily irradiated by 266 nm radiation. From the dichroic filter to the chamber, the beam passed through an iris, the chamber's quartz window, and then was focused behind the surface of the target (to avoid air breakdown) by the use of a 1 inch diameter, 100 mm focal length plano-convex quartz lens. The target was oriented such that the

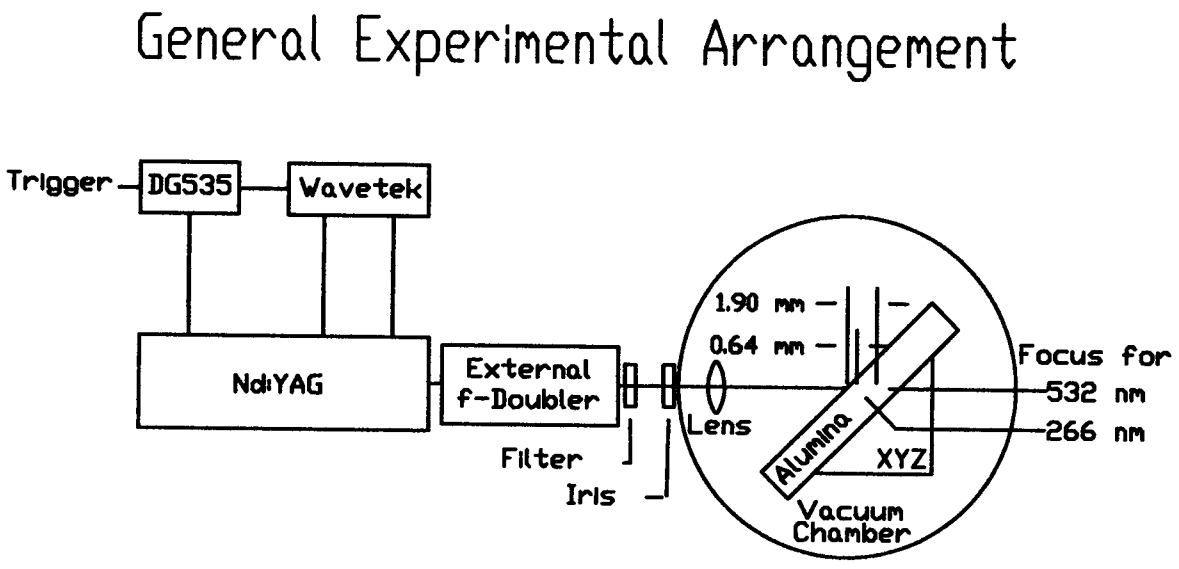

Figure 2: General optical and electronic timing arrangements.

direction perpendicular to its surface was at a 45° angle relative to the direction of the incident laser pulse, which was linearly polarized normal to the plane of incidence. Figure 2 shows the location of the laser focus for 266 nm and 532 nm radiation to be 0.64 mm and 1.90 mm behind the target's surface, respectively. The target sample was mounted on an Oriel model 18011 x-y-z translation stage to provide a virgin target surface for each measurement without any change in focal distances relative to the target surface. When the 532 nm radiation was used, the beam was still put through the external frequency doubler. However, the optimization of the frequency-doubling was intentionally not achieved (crystal angle tuning was misaligned), and the dichroic mirror was removed. The 266 nm and 532 nm radiation at the chamber were measured to have 6.5 mJ and 100 mJ of energy per pulse, respectively. Using the focal points relative to the target surface (assuming geometric optics and no spherical aberrations) gives irradiances of 5 GW/cm^2 and 9 GW/cm^2 for 266 nm and 532 nm radiation, respectively.

2.2 Timing Arrangement

The Nd:YAG laser is Q-switched by the use of a quarter-wave plate, dielectric polarizer, and Pockels Cell along with Q-switching electronics. The Q-switching electronics allows the laser to be externally triggered at the rate of 10 Hz. This external mode option with a rate of 10 Hz is used in all experiments to follow. To accomplish the triggering, a Stanford Research Systems Model DG535 digital delay/pulse generator (DG535) and a Wavetek 50 MHz Model 859 programmable pulse generator were uti-

lized (see Figure 2). Following an input trigger to the DG535, a pulse is sent to the Nd:YAG's external charge input. A second pulse is sent to the Wavetek on a 90 ms delay. The Wavetek then sends appropriately delayed 10 V pulses to the external fire input and to the Q-switch electronics. The externally synchronized laser pulse is generated, and the system then waits for the next triggering of the DG535. With this method, RMS jitter time of less than 2 ns was achieved.

3 Ultra High Speed Photography

3.1 Experimental Setup

Visualization of the laser ablation of alumina was achieved using ultra high speed photography (UHSP) techniques. Figure 3 shows the UHSP experimental setup. The ablation and subsequent plume formation were induced by 266 nm radiation, using the method described in Section 2. The 510 nm radiation of an Oxford Lasers Model CU15A copper vapor laser (CVL) with 30 ns pulses was used as a light source. The CVL irradiated the region of the ablation (parallel to the target's surface) and projected an image of the plume's profile onto a screen, as shown in Figure 3. This image was synchronously photographed by the use of a Weinberger Speed-Cam 512 (WSC) high speed video system. The WSC was operated at 4 kHz, which corresponds to an image resolution of 64x512 pixels. The CVL was triggered synchronously by the WSC. The 4 kHz synchronous output signal of the WSC was also divided by 400 by the use of the trigger and gate output of an oscilloscope. The resulting 10 Hz signal was sent to the DG535 for the synchronization of the Nd:YAG.

3.2 Experimental Results

Figure 4 shows a sequence of shadowgraphs taken by the use of UHSP. The first shadowgraph shown in Figure 4 was taken coincident with the arrival of the laser pulse on the target (zero time). Between the first and second shadowgraphs, the laser ablation and corresponding induced plasma is created and begins to cool. At 250 μs after the laser pulse, a shock wave (dissipating the mechanical energy induced by the

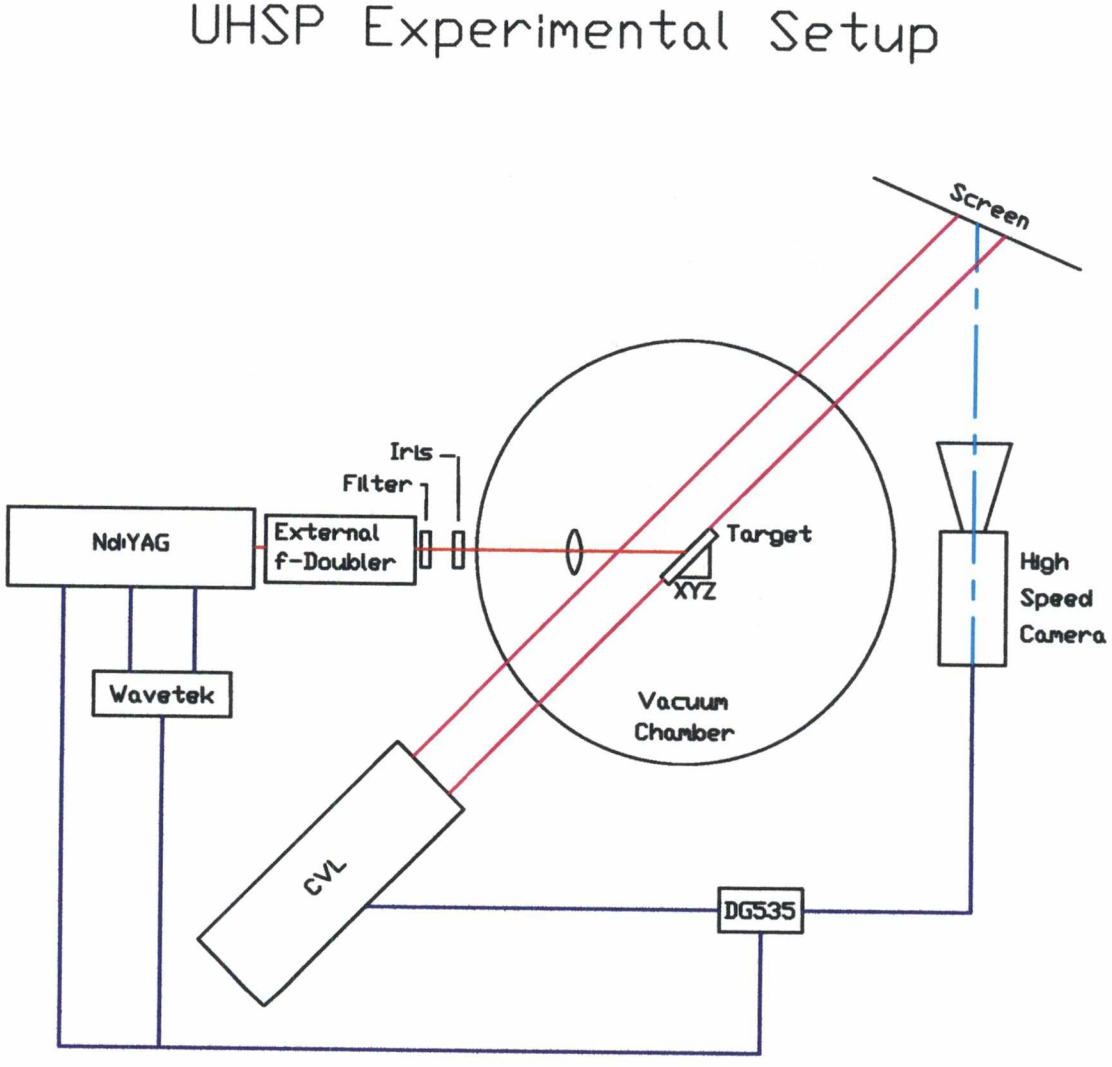

Figure 3: Ultra high speed photography experimental setup.

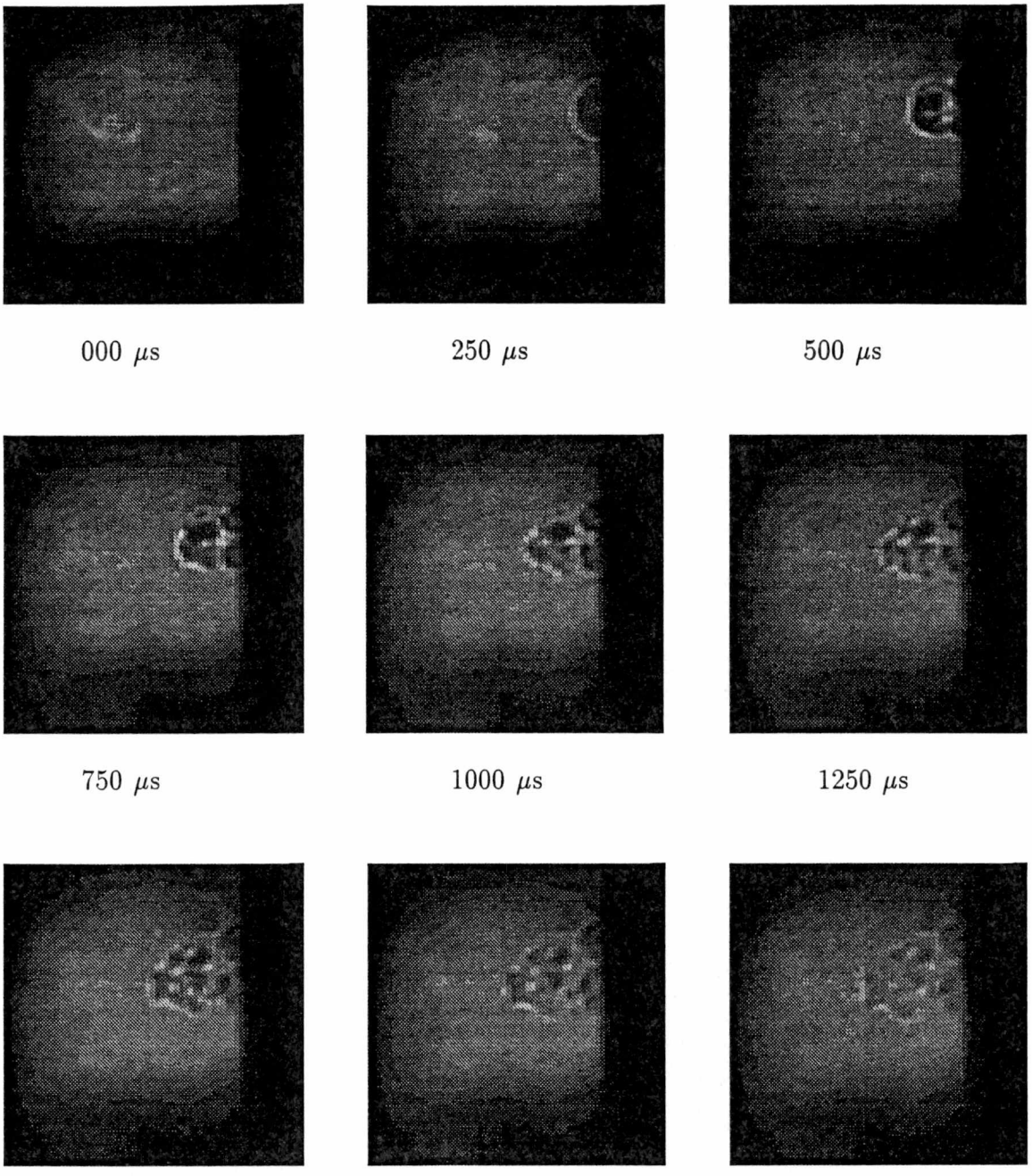

Figure 4: Ultra high speed photographic results.

laser pulse) propagates away from the target as shown in the second shadowgraph. Figure 4 also displays in the remaining shadowgraphs the turbulence of the mixing of the ablated material with the ambient atmosphere after the passage of the shock wave.

4 Mass Spectroscopy

The intent of this section is to understand the composition of the target and the products of the laser ablation of alumina. The target composition is determined by the use of a scanning electron microscope (SEM) along with a x-ray detector. A quadrupole mass spectrometer is applied in the attempt to measure the plume composition.

4.1 Target Composition

The target used was a 99.5% alumina tile from Coors Ceramics. Some physical properties of the target are shown in the Appendix. From verbal communications with Coors Ceramics, it was learned that several oxides exist as impurities. Table 1 displays the stated specific impurities and the maximum concentrations by mass. With the use of a scanning electron microscope and a x-ray detector, the presence of Al, Si, Mg, Ca, and Fe in decreasing order were verified. The amount of aluminum detected by the scan was expected to be dominant, and it should be noted that the range of the elemental scan was set to ignore the presence of oxygen [15].

Table 1: Composition of the alumina target

Species	Composition
Al_2O_3	99.5%
SiO	<0.2%
MgO	<0.1%
CaO	<0.1%
FeO	<0.1%
NaO	<0.1%

4.2 Experimental Setup

An attempt was made to use mass spectroscopy to observe the products of laser ablation of the alumina target. Using a EAI/QUAD Model 1100A quadrupole mass spectrometer (QMS) with a 1 amu resolution, the composition of the gas near the impact point of the 266 nm radiation was measured. Due the requirements of the QMS, the pressure of the vacuum chamber was held at 10^{-6} Torr by the use of a Balzers water-cooled cryogenic pump and two standard roughing pumps. The pressure of the vacuum chamber was continuously measured by a Granville-Phillips Series 260 gauge controller and an ion gauge.

The QMS gives the user the ability to vary the scan time, the center mass, and the mass range. For this particular experiment, the scan time was set to 50 s, and the center mass and mass range were set such that the scan covered from about 1 to 50 amu. This gave an integration of about 1 amu per second. The output of the QMS was viewed by a Tektronix Model 2225 oscilloscope and recorded by a Kipp & Zonen strip chart recorder type BD122.

4.3 Experimental Results

Figure 5 shows a typical result of the mass spectroscopy experiment. The top graph shows the background mass spectrum, which was taken with the laser blocked. The bottom graph shows the mass spectrum taken during the laser ablation process. The positions of the H, C, N_2, O_2, and AlO are labeled by 1, 12, 28, 32, and 43 amu, respectively. The wide peak centered at 15 amu is due to the large quantities of N

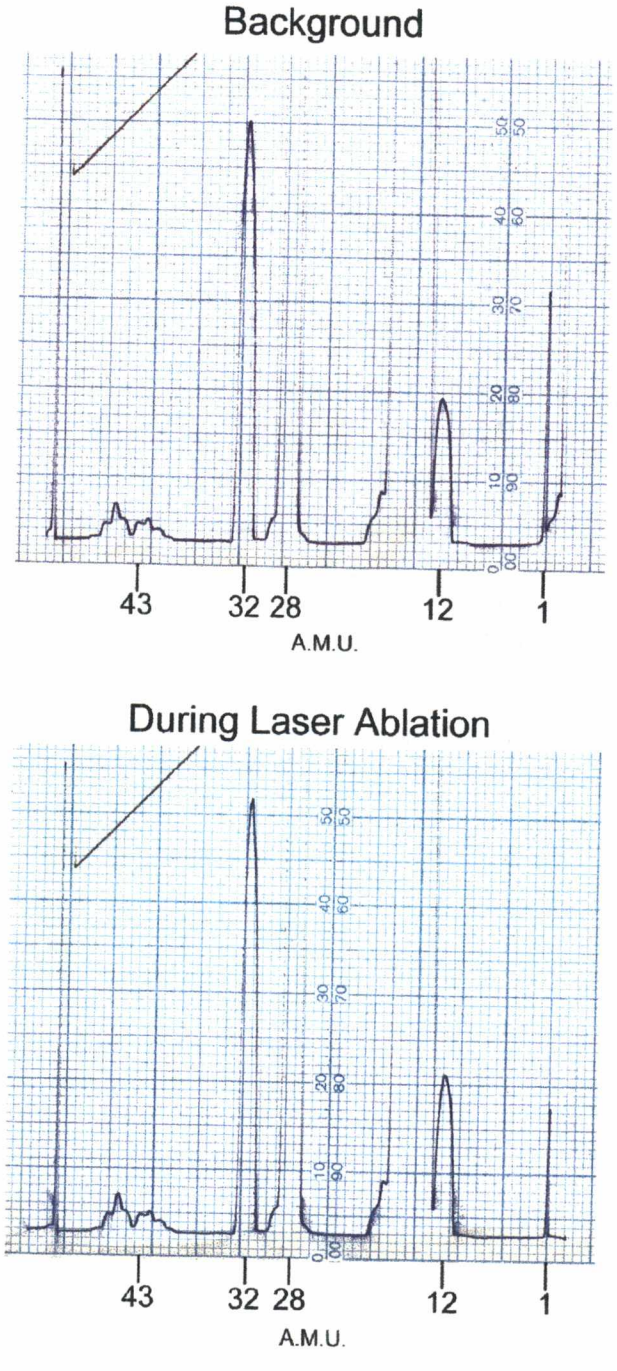

Figure 5: Mass spectroscopy results.

and O. Resolving these lines would cause a decrease in the intensity resolution. Since the less concentrated species such as AlO are of interest, the intensity resolution was most important. The peaks in the 40 to 48 range surrounding AlO are partially due to the hydrocarbons which are introduced to the vacuum chamber by the pump oil [16]. Comparing the mass spectroscopy data during laser ablation with that of the background, negligible differences are found. Hence, the detection of the composition of the plume was not achieved.

Ablation products such as Al and O are not easily detected due to the high intensities of N_2 and O in the background. In addition, Si, Mg, Ca, Fe, and Na are not detected because of their low concentrations in the target sample. The distance between the QMS and the impact point gives rise to additional losses in the sensitivity due to the extremely small solid angle subtended by the QMS aperture at the target and plasma regions. With the assumption that O_2 contributes to 1% of the background, the sensitivity of the detection was on the order of parts per ten thousand. Finally, although the QMS single mass monitoring capabilities were used, the products of ablation were not detected.

As reported by Ching, Gilgenbach, and Lash [8], the AlO formation by chemical recombination is favored at high ambient pressures and the AlO emission approaches a linear dependence for pressures greater than 200 mTorr. Therefore, it is reasonable that AlO formed by this mechanism was not measured by the QMS at pressures of 1 μTorr. Additionally, since no AlO signal was observed, there was no detection of AlO produced directly from the Al_2O_3 sample from photodissociative ablation.

5 Optical Spectroscopy

This section contains the major experimental focus of the work. Optical spectra are recorded of the expanding and cooling laser-induced plasma over a wavelength range of 420 nm to 560 nm and for various time delays and gate widths. The experimental setup required to achieve the time-resolved measurements of the optical spectra and an analysis of the results are presented.

5.1 Experimental Setup

The experimental setup for measuring the optical spectroscopy of laser-ablated alumina uses the laser system described in Section 2. The DG535 delay generator is triggered by a EG&G PARC Model 1460 optical multichannel analyzer (OMA). Figure 6 shows the basic experimental setup and the physical positioning of the target. The optical emission of the laser-induced plasma was collimated and focused onto a nominal 250 μm slit of a 0.275 m Jarrell-Ash crossed Czerny-Turner spectrometer by two lenses selected to optimize the f/#. A 350 nm cut-on filter was used to avoid possible complications from second-order diffraction of uv plasma emission lines. The AlO spectrum was measured by the use of an EG&G PARC Model 1241 intensified linear diode array (LDA) and read with the OMA. The OMA was programmed such that the LDA was read synchronous to the laser repetition rate (10 Hz).

After the LDA read-out and before the next laser pulse, dark-count noise is accumulated by the LDA. To reduce this between-pulse dark-count build-up, the detector

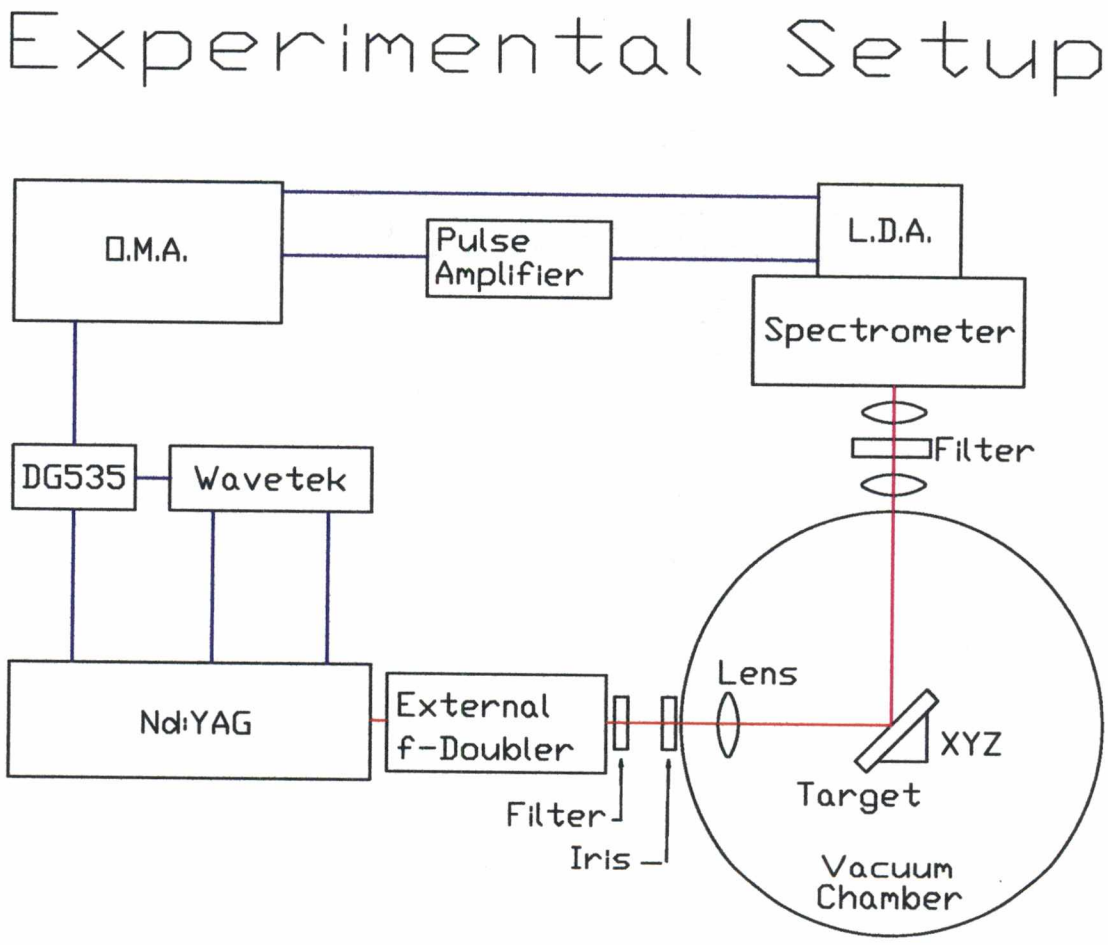

Figure 6: Optical spectroscopy experimental setup.

was cooled to 5°C and four additional read-outs, or pixel charge neutralizations, were performed. The desired time resolution was accomplished by applying a high voltage pulse to the microchannel intensifier that is coupled to the input face of the LDA. At selected time delays after the laser pulse, the OMA triggered an EG&G PARC Model 1304 pulse amplifier, which provided the high voltage pulses to the microchannel plate.

Each measurement consisted of 50 laser pulses, which provided an averaging function for various random fluctuations, reducing the fluctuations in the result by about 14%. A virgin sample was provided to each set of 50 pulses by translating the target surface using an Oriel Model 18011 translation stage. The focal area was unchanged by the sample translation.

The measured spectra underwent three calibrations to remove systematic errors: wavelength, intensity, and dynamic. The wavelength calibration was performed with the use of atomic hydrogen spectral lines. This allowed for the correlation between the pixel number and wavelength of incident radiation. The intensity calibration was accomplished by the use of a tungsten lamp. Differences between the measured and known spectra were used to obtain the appropriate scaling factor for the intensity at each pixel. The intensity calibration was done with a gate width of 10 μs. Finally, the wavelength shift due to the non-linearity of the spectrometer was accounted for by a dynamic wavelength calibration.

Table 2 shows the specification of timing errors that originate and propagate in

the gate pulse interface and the pulse amplifier. From the table, it is clear that the error in the time delay resulting from the gate pulse interface is on the order of 2% of the gate width, and approximately 40 ns of uncertainty can be attributed to the pulse amplifier. Since the range of time delays started at 0 ns, the error due to the propagation delay of the pulse amplifier must be considered. With the minimum gate width of 200 ns, the effect of this error is not critical since the gate width inherently creates a loss of time resolution. From Table 2, the error in the gate width due to the gate pulse interface is 3%, and that due to the pulse amplifier is on the order of 18% for our minimum gate width setting. The two sources combine to give a 35% error. However, the required temporal resolution for the experiment is much less than that of the errors described.

5.2 Time-Resolved Spectroscopic Results

Table 3 displays a partial listing of the laser radiation wavelength, time delay after laser impact on the target, and gate width for the data. An example of the data recorded at selected time delays is shown in Figure 7. We are now able to expand upon the chronology of the plasma expansion obtained using ultra high speed photography. From the spectral lines detected at the 0.8 μs delay, it is observed that the plasma has cooled sufficiently to allow the atomic formation of atoms by ion-electron recombination. The atomic lines of Ca, Mg, and H have been identified in top spectrum of Figure 7, 0.8 μs after the initial laser-surface interaction. The 466 nm atomic line remains unidentified. It is interesting to note that, for a pure hydrogen plasma, the

Table 2: Timing error of the measurement components

Gate Pulse Interface (1303) [17]	
Insertion Delay	
70(5) ns programmable delay in	
30(5) ns programmable delay out	
Delay Specifications	
Range	[0 to 13.1 ms] +insertion delay
Resolution	1 ns
Accuracy	2% of setting - insertion delay
Jitter	greater of 100 ps or 0.02% of delay
Pulse Width Specifications	
Accuracy	3%
Jitter	0.1% of pulse width
Range	Resolution
100 ns to 1 μs	5 ns
1 μs to 10 μs	50 ns
10 μs to 100 μs	500 ns
100 μs to 1 ms	5 μs
1 ms to 10 ms	50 μs
Pulse Amplifier (1304) [18]	
Propagation Delay	
40 ns from trigger input to gate output	
Fall Time	
Less than 20 ns	
Rise Time	
Gate Width Range	Rise Time
100 ns to 1 μs	$<$ 50 ns
1 μs to 10 μs	$<$ 500 ns
10 μs to 100 μs	$<$ 1 μs
100 μs to 1 ms	$<$ 10 μs
1 ms to 10 ms	$<$ 100 μs

Table 3: Resolved spectroscopic measurements.

Wavelength nm	Time delay μs	Gate width μs
266	0.0	0.2
266	0.2	0.2
266	0.4	0.2
266	0.6	0.2
266	0.8	0.2
266	1.0	0.2
266	1.0	1.0
266	2.0	1.0
266	3.0	1.0
266	4.0	1.0
266	5.0	1.0
266	6.0	1.0
266	7.0	1.0
266	8.0	1.0
266	9.0	1.0
266	10.0	1.0
266	20.0	10.0
266	20.0	10.0
266	20.0	10.0
532	20.0	10.0
266	30.0	10.0

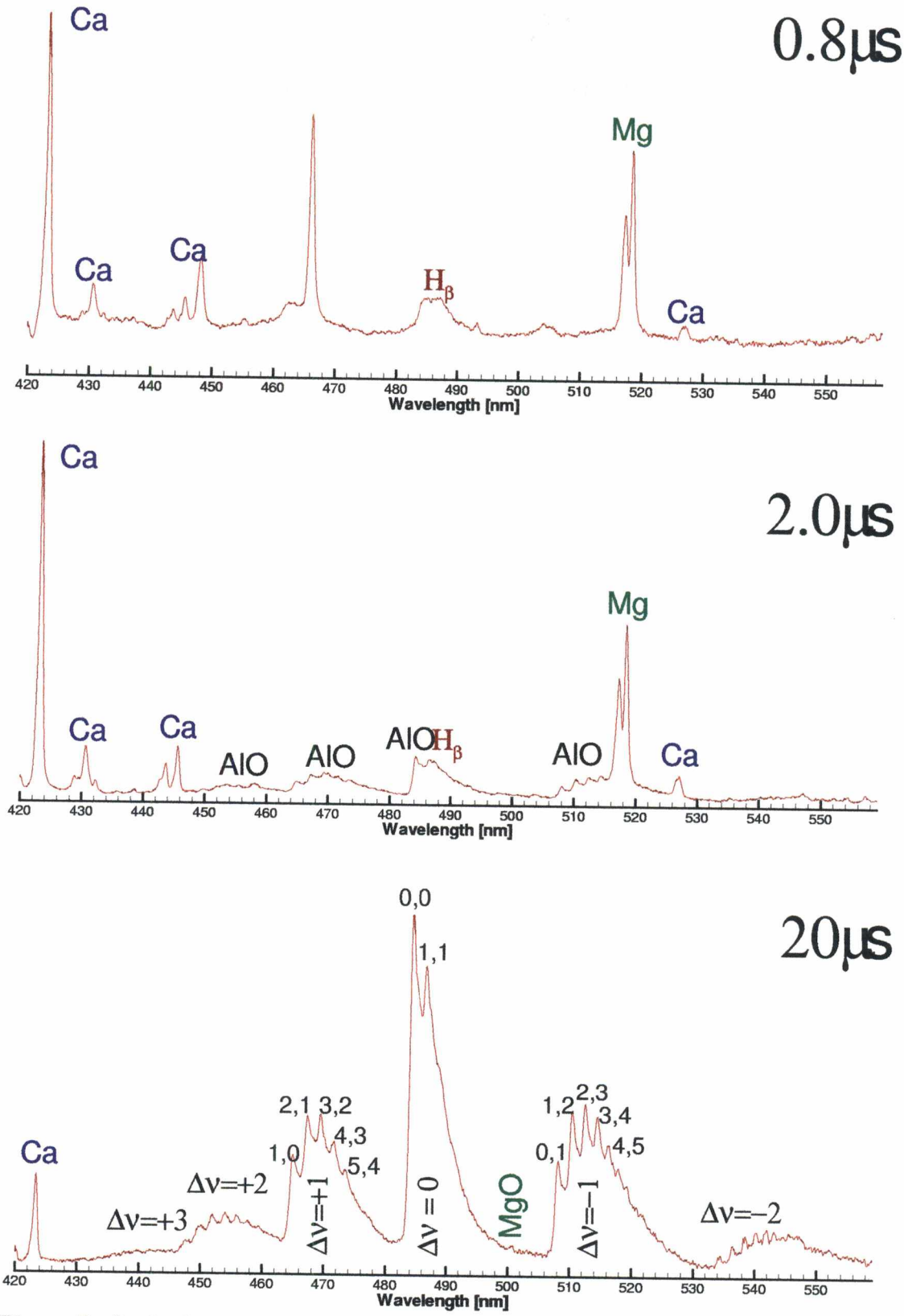

Figure 7: Optical spectroscopy results for 0.8, 2.0, and 20 μs time delays.

observed width of the Stark broadened H_β Balmer series line would yield an electron number density on the order of 10^{17} cm^{-3} and a temperature of approximately 11,000 K [19]. The Ca and Mg line positions and intensities may also be used to measure the plasma temperature and electron number density, but experimental data with higher resolution would be required. It is recalled from the composition of the target that the Ca and Mg spectral lines are expected. The H_β line may not expected since the target is supposed to have 0% water absorption, but the precision of this specification is unknown. After 2 μs AlO is starting to form, as seen by the middle spectrum in Figure 7. At 20 μs following the plasma formation, the AlO $B^2\Sigma^+ \longrightarrow X^2\Sigma^+$ molecular transition is seen to dominate the spontaneous emission signature. In this spectrum, shown on the bottom of Figure 7, the bands corresponding to a change in vibrational quantum number of 3, 2, 1, 0, -1, and -2 are shown, and some individual vibrational transitions are labeled. The only spectral impurities in the observed AlO wavelength region at this time delay are those of Ca and MgO, with the latter questionable.

6 Temperature Determination

In this section, the AlO spectra observed at 20 μs following the laser irradiation of the target are used to infer the temperature of the expanding gas. Both 266 nm and 532 nm incident laser irradiation are used to produce the plasma. The temperature of the assumed local-thermal-equilibrium (LTE) gas is determined using two different analysis methods. A comparison of the results will be shown.

6.1 Theory

The basis for the numerical determination of the temperature from measured spectral signals is the minimization of the sum of the squared-residuals from the measured and calculated spectral signals. Therefore, a requirement for the determination of T is the ability to predict the theoretical spectra over a range of temperatures. For this study, a theoretical, or synthetic, spectrum is needed for the AlO $B^2\Sigma^+ \longrightarrow X^2\Sigma^+$ transition system. This synthetic spectrum was obtained using the line strength file (LSF) for this electronic transition. The LSF is an electronic table which contains all the information required to calculate radiative transitions. The information includes term values, line strengths, quantum numbers, and parities [20]. For diatomic molecules, the parameters required to create the LSF are B_v, D_v, T_e+G_v, S, and J_{max} for all vibrational states (of both the upper and lower electronic states) to be considered. The first two parameters are the coefficients of the first two terms in the rotation term value:

$$F(J) = B_v J(J+1) - D_v J^2(J+1)^2 + H_v J^3(J+1)^3 + ..., \quad (1)$$

where J is the rotational quantum number. The third parameter is the sum of the electronic and vibrational term values:

$$T_e + G_v = T_e + \omega_e(v+\frac{1}{2}) - \omega_e x_e(v+\frac{1}{2})^2 + \omega_e y_e(v+\frac{1}{2})^3 + ..., \quad (2)$$

where v is the vibrational quantum number. The fourth parameter, S, is the total spin of the state. J_{max} is the maximum rotational quantum number to be considered.

The first four parameters are easily extracted from published papers such as Coxon and Naxakis [21, 22, 23]. The J_{max} parameter was approximated by requiring a 10,000:1 intensity ratio between the 0,0 band head and the smallest rotational transition to be considered. With these parameters for each vibrational transition, the LSF is computed by the use of Rydberg-Klein-Rees (RKR) algorithms [24] and Hamiltonian diagonalization methods [25]. The LSF used contains the information on over 33,000 molecular transitions of AlO.

Using the LSF, it is possible to calculate the coefficients of the vibrational term value. From the LSF, we find that the vibrational coefficient ω_e for the upper and lower states are 871 and 979 cm^{-1}, respectively. In addition, the vibrational coefficient corresponding to the first anharmonic term $\omega_e x_e$ for the upper and lower states are 3.70 and 7.03 cm^{-1}, respectively. Table 4 compares these values with those previously measured [23]. The influence of the anharmonic term can best be investigated by computing the energy deviations due to the $(v+\frac{1}{2})^2$ perturbation term. Figure 8

Table 4: Comparison of calculated and measured values of ω_e and $\omega_e x_e$.

	Derived		Measured[23]	
	Upper state	Lower state	Upper state	Lower State
$\omega_e[\text{cm}^{-1}]$	871	979	870.44(4)	979.52(7)
$\omega_e x_e[\text{cm}^{-1}]$	3.70	7.03	3.668(3)	7.030(8)

displays the results graphically. As seen in Figure 8, the vibrational energy of a molecule with vibrational quantum number of 10 has harmonic and anharmonic values that differ by 5% and 8% in the upper and lower state, respectively. Thus, it is necessary to carry the approximation of the potential curve out beyond the first term.

To create a synthetic spectrum, only the temperature of the molecule and the experimental full-width at half maximum (FWHM) spectral resolution are required. This may easily be seen by looking at the Boltzmann distribution, which relates intensity to energy:

$$I_{mn} = (constant) G_m A_{mn} \nu_{mn} e^{-E_m/kT}, \tag{3}$$

where I_{mn} is the intensity of radiation emitted from a state m to state n transition, G_m is the degeneracy of the state m, A_{mn} is the Einstein coefficient for spontaneous emission, ν_{mn} is the frequency of radiation emitted due to the state m to state n transition, E_m is the energy of state m, k is the Boltzmann constant, and T is the temperature. Notice that all the variables are contained in the LSF except for temperature.

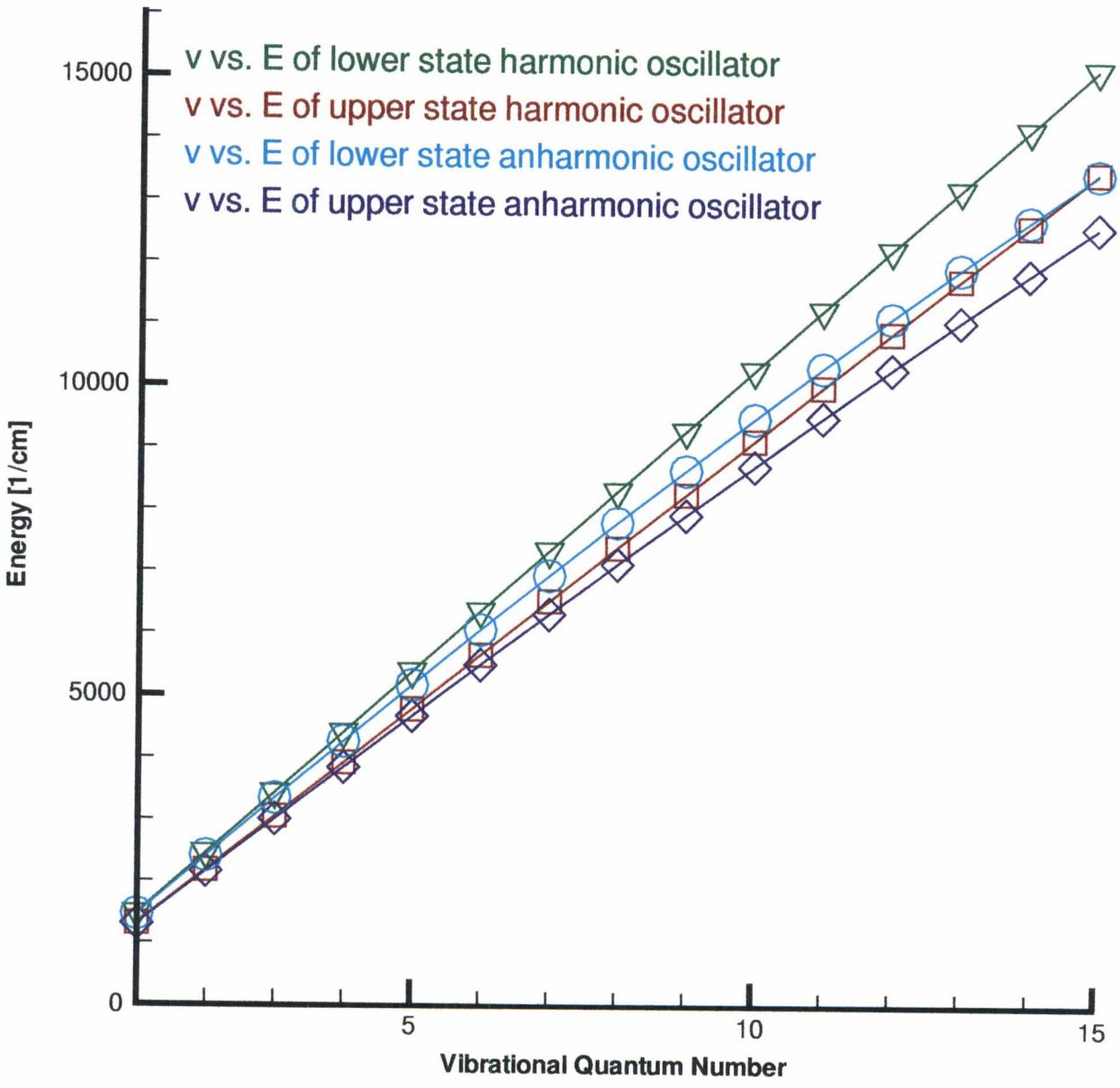

Figure 8: The harmonic and anharmonic vibrational energy term values.

6.2 Temperature Extracting Algorithms

Two ways of extracting the temperature from a spectrum by the use of Equation 3 will be investigated. The first method is called NMT (Nelder-Mead Temperature), and the second is called DBP (Diatomic Boltzmann Plot). NMT finds the synthetic spectrum that best fits the intensities of the entire experimental spectrum by the minimization of the sum of the squared residuals using the Nelder-Mead minimization algorithm. The temperature of the optimum synthetic spectrum is taken to be that of the experimental spectrum. DBP selects only certain peaks of the spectrum and performs a modified Boltzmann plot using the data of these peaks. Although the two methods are both based on Equation 3 and both use the same parameters obtained from the LSF, the results can be expected to differ slightly due to the different way each is affected by noise and systematic errors.

In the implementation of DBP, problems may arise in the peak finding algorithm when the influence of noise is present. Noise may cause the shift of a peak's intensity and position, or even create the appearance of peaks that do not exist. These variations from the 'true' spectra may cause drastic differences in the temperature determination due to incorrect evaluations of the modified Boltzmann plot parameters. Thus, one must be able to differentiate between a true peak and an effect of noise. To this end, a 15-point 6-degree Savitzky-Golay filter (SGF) was used. The advantage of such a filter is that loss of spectral resolution is minimal and the shift in wavelength due to the filter is negligible [26]. With the filtered spectra, finding

the peaks may be accomplished by the use of a simple algorithm (such as a series of conditional statements). Hence the peak finder is also a filter, and consequently the potency of the SGF and the peak finder must be adjusted so that the two best complement each other. Over-filtering of the data must be avoided because it would induce an error. Trial and error with visual comparison of raw and filtered data was involved in picking a 15-point 6-degree SGF. With the wavelength position of a peak found, the intensity of the peak may be taken to be that corresponding to the original or filtered data. Both methods will be applied in the DBP method.

The precision of the derived temperatures was determined by a Monte-Carlo simulation as follows: An experimental spectrum was analyzed to find the temperature by each of the methods. The noise in the experimental spectrum, determined from the quotient of the experimental spectrum and its filtered counterpart, yielded an estimate of 3% random noise. A further 3% of random noise was added to the experimental spectrum, which was then reanalyzed by each method. Repeating the process 10,000 times produces a Gaussian distribution of temperatures. The standard deviation of the distribution was taken to be the precision of the experimentally measured temperatures.

6.3 Determined Temperatures

The 20 μs time delay spectrum from 430 nm to 540 nm was selected for the temperature analysis of AlO to ensure minimal, non-random background contributions arising from the atomic lines. Figures 9 and 10 show the application of the temper-

ature extracting algorithms to an experimental spectrum created by the 266 nm and the 532 nm irradiation, respectively. The spectral fits are the synthetic spectra with the determined temperature and FWHM of the experiment. The results of taking the filtered versus the measured peak intensities in the DBP method are shown to overlap (and hence the green curves are hidden by the purple curves in Figures 9 and 10). This may be taken as an indication that the SGF did not bias locations and intensities of the experimental spectra.

Figure 11 illustrates typical characteristics of the NMT spectral fitting. This figure specifically shows the difference in the fits for the various methods and wavelengths of irradiation. The residuals of the fits lie almost entirely within 10% relative to the respective 0,0 peak intensity. Several interesting conclusions may be drawn from this figure. First, the residuals of the individual sequences show oscillatory behavior due to inaccuracies near spectral peaks. Second, the residuals for the AlO progressions yield an apparent low frequency oscillation, which is represented by the red dotted line, obtained by a 201-point 6-degree SGF on the residuals. The low wavelength region of the 266 nm data (top plot) indicates more positive residuals, or a higher computed intensity distribution, for the Δv=+3 sequence. In turn, this region is well predicted for the 532 nm data (residuals are approximately zero). The Δv=+2 and Δv=+1 sequences appear to be under predicted, while the Δv=-1 theoretical sequence appears to be well matched to the data. Note that the residual of the Δv=0 sequence is approximately centered around zero, yet the intensities near 484 nm and

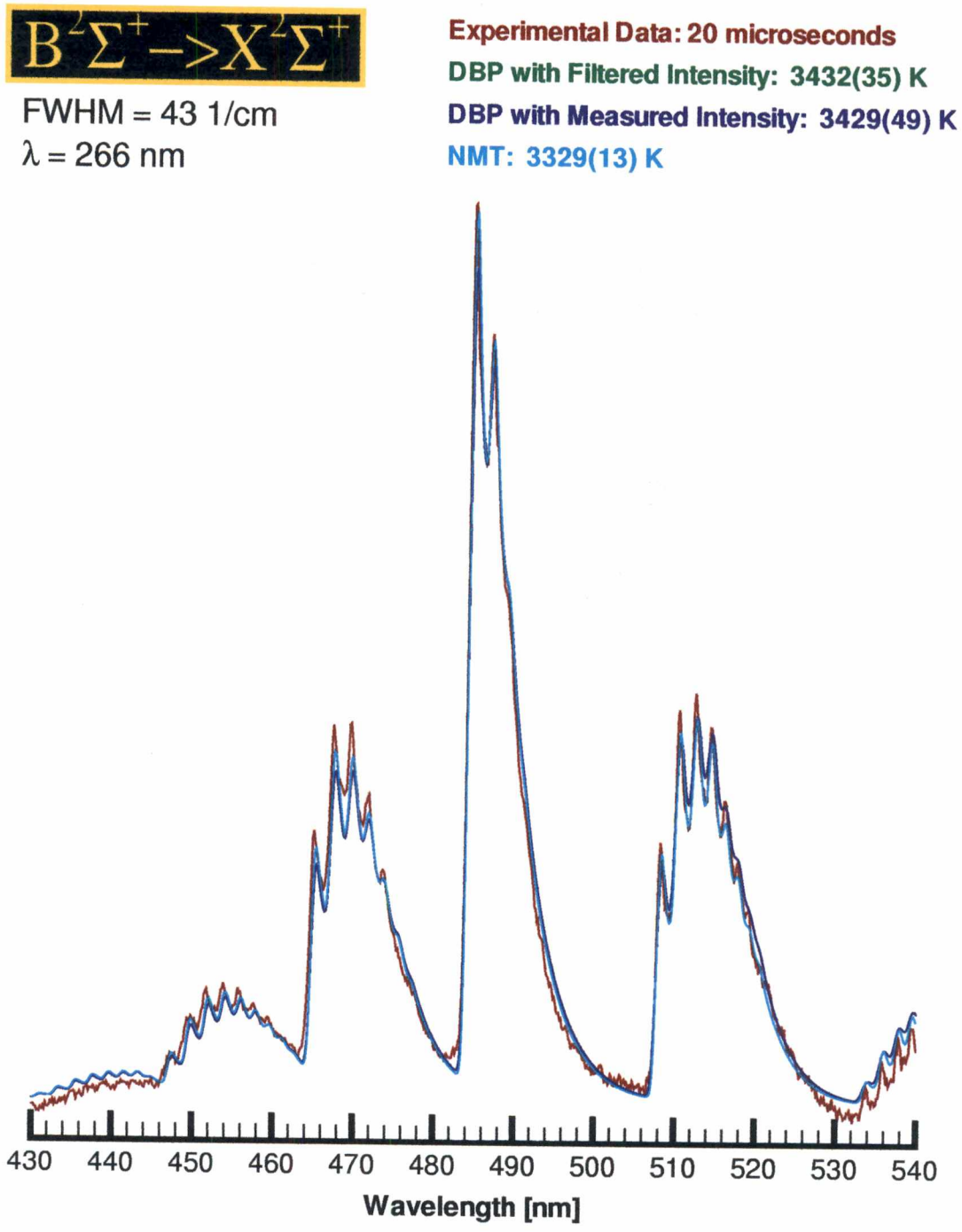

Figure 9: Temperature determination for 266 nm irradiation.

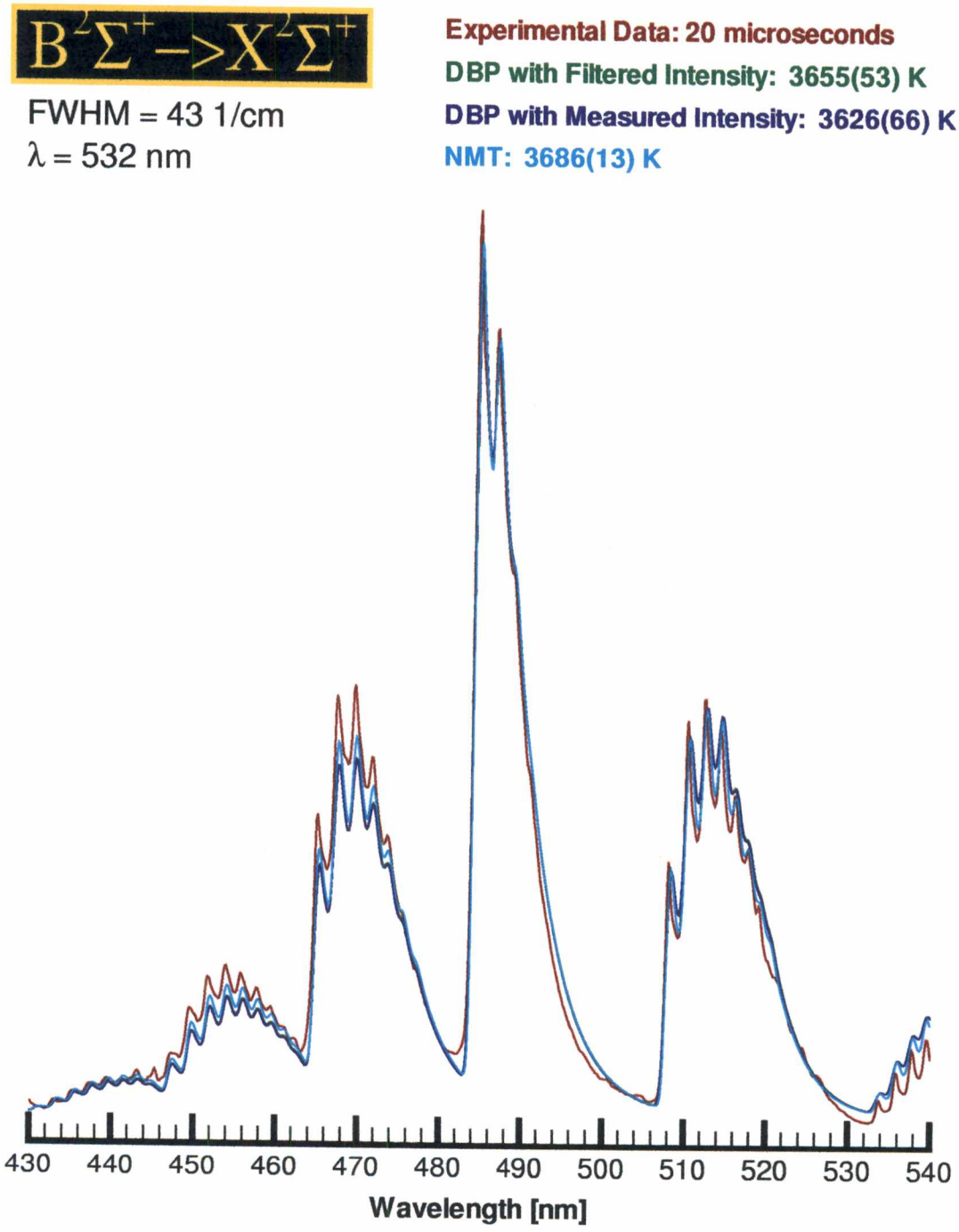

Figure 10: Temperature determination for 532 nm irradiation.

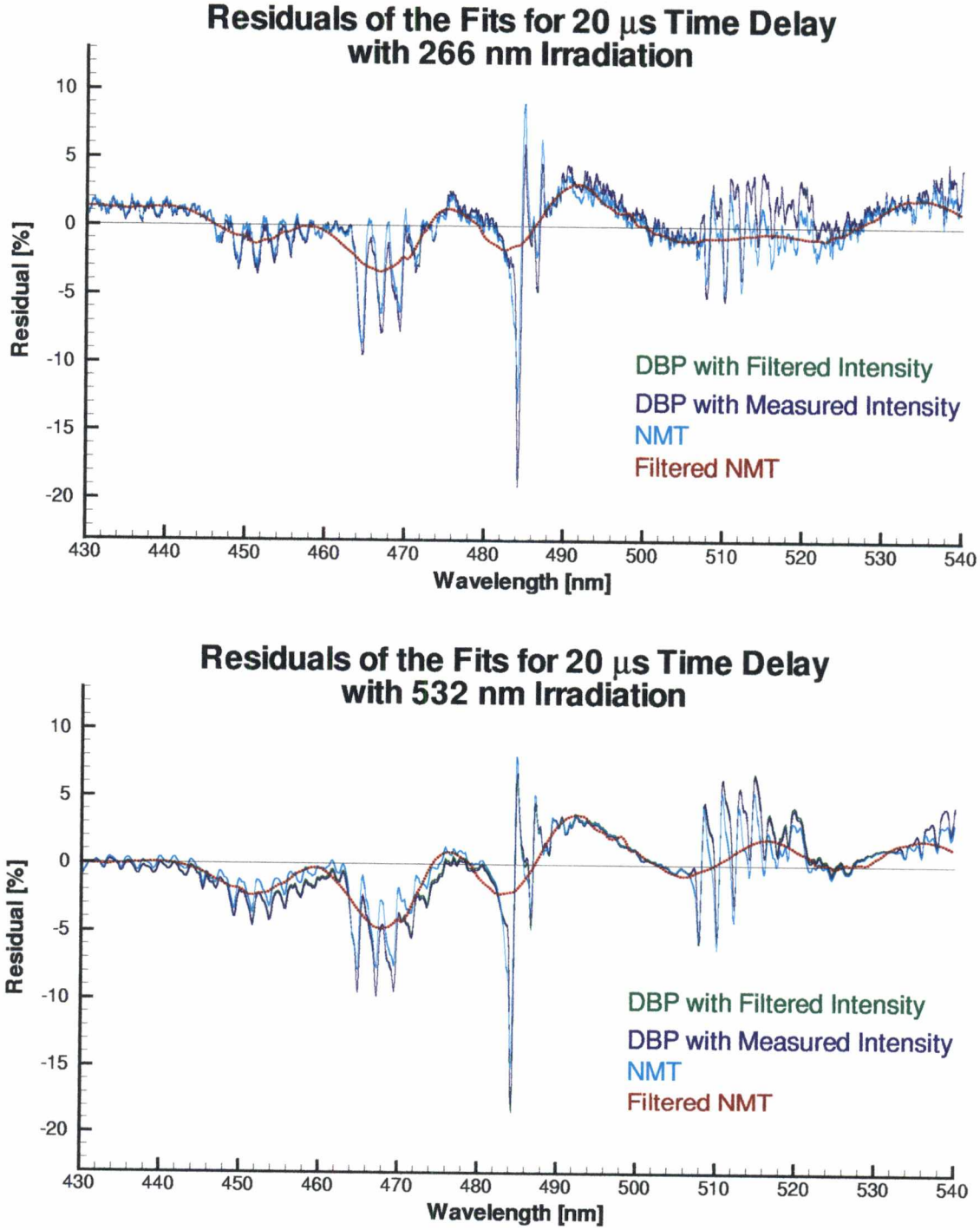

Figure 11: Difference of fitted and measured spectra relative to the intensity of the 0,0 band.

500 nm are under- and over-predicted, respectively. In addition, Figure 11 displays the residuals for the DBP method. The DBP residuals are computed by the use of the synthetic spectra that is obtained from the inferred DBP temperature. It is possible that similar behaviors of the residuals in the top and bottom plots are due to wavelength dependent background contributions.

The top plot in Figure 12 shows the peaks selected by the peak finding method in the 266 nm irradiation spectra. The bottom plot of Figure 12 displays the modified Boltzmann plot created with the selected peaks. The standard deviation of the DBP found by the Monte-Carlo simulation is on the order of 1% of the temperature, which is approximately a factor of 6 better than in prior work [27]. The addition of the SGF and better peak finding techniques to DBP are credited for this improvement. The determined spectral temperatures using DBP and NMT are within two standard deviations of each other, which quantifies the level of agreement among the methods. Additionally, for the 532 nm irradiation the temperature agreement is found to be within one standard deviation. The 532 nm spectrum has intensities 30 times greater than the 266 nm due to the increased irradiance

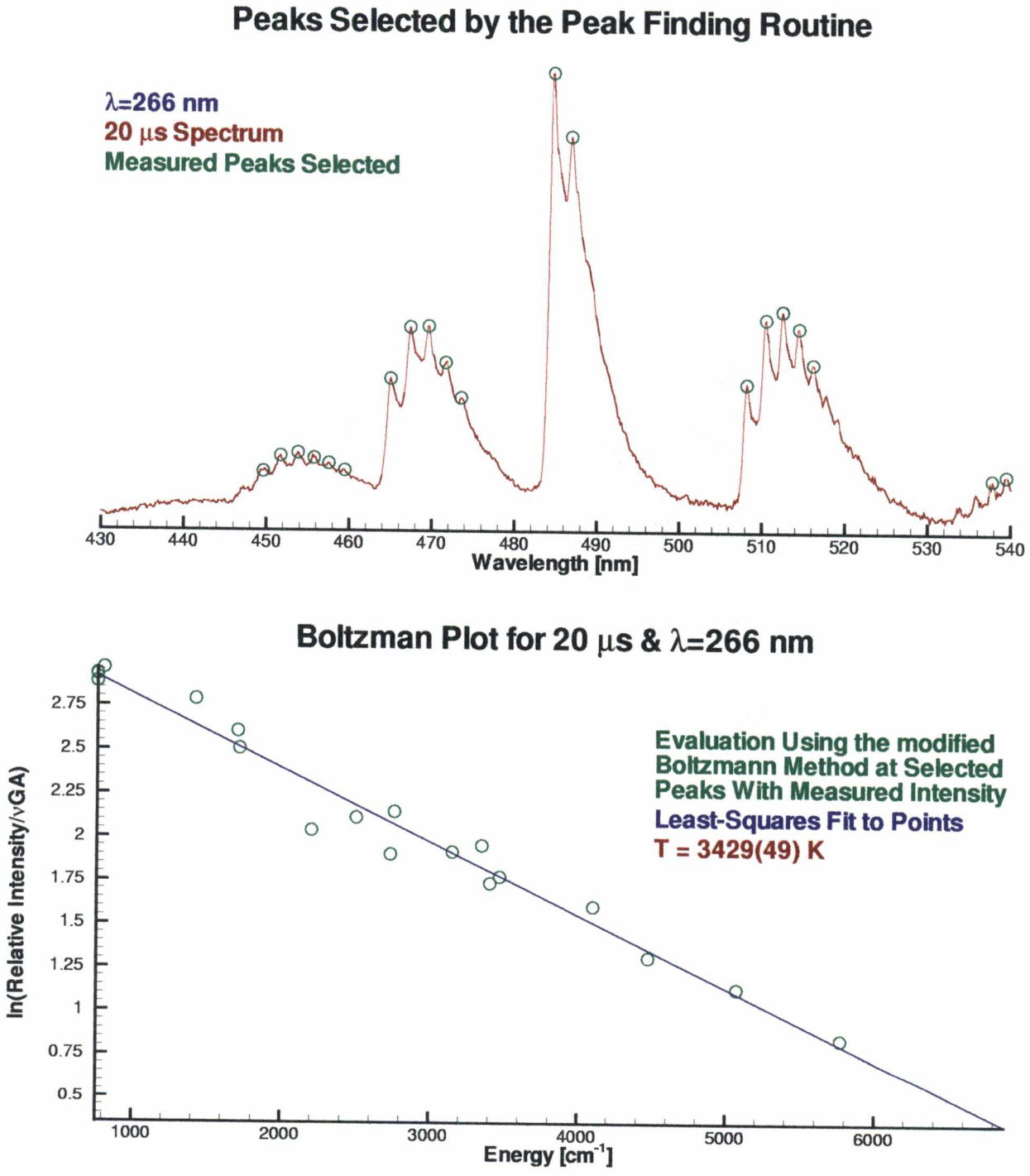

Figure 12: Modified Boltzmann plot for selected peaks.

7 Conclusion

Measurements of the laser ablation of alumina are important not only for the study of laser surface interaction, but also for the understanding of the aluminum monoxide (AlO) blue-green $B^2\Sigma^+ \longrightarrow X^2\Sigma^+$ band system. Spectra have been computed by the use of accurate diatomic line strengths and measured in experiments using short-pulse, high peak power laser ablation of alumina. Incident laser irradiances on the order of 5 GW/cm^2 were used. In this work, the measurement techniques used to investigate the laser ablation of alumina included ultra high speed photography (UHSP), scanning electron microscope with x-ray detection (SEM), quadrupole mass spectroscopy (QMS), and time-resolved optical spectroscopy.

The UHSP allowed the sequence of events following an individual laser pulse interaction with the target sample's surface to be recorded. The SEM applied to the alumina target confirmed the existence of impurities in the target as detected in the early time delay optical spectra. The composition of the plume could not be determined by the QMS for a variety of reasons including the level of sensitivity and the intensity of the background. With the time-resolved optical spectra of the decaying plasma, a chronological understanding of the plume composition was obtained. Also, with the use of the H_β Balmer series line a temperature of typically 11,000 K and number density of typically 10^{17} cm^{-3} at a 0.8 μs time delay can be inferred. The formation of AlO was measured as early as 2.0 μs, and became nearly pure at 20 μs after the laser impact. NMT and DBP algorithms were applied to the spectra of 266

nm and 532 nm laser ablation at a 20 μs time delay. With DBP, a 15-point 6-degree SGF was implemented in the peak finding process. The precision of the temperature calculations were determined from a Monte-Carlo simulation. The result was temperatures well in excess of 3,000 K with a precision on the order of 1%, and agreement between methods within 2 standard deviations. However, the fit shows signs that the background is not flat, possibly indicating the presence of unknown systematic errors. The line strength file and ability to characterize various plasma phenomena make the methods used in this thesis useful in diagnostics applications to describe gas dynamic plume effects.

8 Future Research

There are two major areas of interest that should be investigated. The first area is experimental investigation of the wavelength-dependent background contribution and application of a method to account for it in the analysis (possibly including the atomic lines of the impurities). The second area is in the weighting of each pixel according to the reliability of the information content. The use of weights would result in less emphasis to be placed on regions where the spectral noise is comparatively large. The development of techniques in these two areas should result in better spectral fits along with a more accurate determination of the spectral temperature for all time delays. This would allow for the extraction of the temperature decay over increasing time delays to further characterize the laser ablation of alumina.

Other areas of interest include femtosecond pulse laser ablation and ultra high speed holographic photography of the plume. Ultimately, a real-time temperature measuring device using the methodology and algorithms described could be implemented. Such a device could be applied to determine the temperature of AlO in processes ranging from rocket exhaust to the welding of aluminum.

References

References

[1] Herzberg. *"Spectra of Diatomic Molecules"*. D. Van Nostrand Company, Inc., New York, 1963.

[2] Marcel Vanpee, William R. Kineyko, and Ronald Caruso. "Experimental Determination of the Oscillator Strenths for the $A^2\Sigma^+ \longrightarrow X^2\Sigma^+$ Band System of Aluminum Oxide". *Combustion & Flame*, 14:381–395, 1970.

[3] Ove Harang. "Excitation of AlO Bands in the Sunlit Atmosphere and the Determination of the Temperature From the Distribution Among the Vibrational Levels". *Planetary Space Sci.*, 12:567–571, 1964.

[4] R. W. Nicholls, W. Parkinson, and E. M. Reeves. "The Spectroscopy of Shock-Excited Powered Solids". *Appl. Opt.*, 2:919–930, 1963.

[5] I. K. McDonald and K. K. Innes. "A Low-Lying Excited State of the AlO Molecule and the Ground-State Dissociation Energy". *J. Mol. Spectrosc.*, 32:501–510, 1969.

[6] V. W. Goodlett and K. K. Innes. "Hollow-Cathode Emission of the AlO Spectrum". *Nature*, 183:243–244, 1959.

[7] Chikashi Yamada, Edward A. Cohen, and Eizi Hirota. "The microwave spectrum of the AlO radical". *J. Chem. Phys.*, 92:2146–2149, 1990.

[8] C. H. Ching, R. M. Gilgenbach, and J. S. Lash. "Detection of AlO molecules produced by KrF laser-ablated Al atoms in oxygen gas and plasma environments". *J. Appl. Phys.*, 78:3408–3410, 1995.

[9] Hongxin Wang, A. P. Salzberg, and Brad R. Weiner. "Laser ablation of aluminum at 193, 248, and 351 nm". *Appl. Phys. Lett.*, 59:935–937, 1991.

[10] R. W. Dreyfus, Roger Kelly, and R. E. Walkup. "Laser-induced flourescence studies of excimer laser ablation of Al_2O_3". *Appl. Phys. Lett.*, 49:1478–1480, 1986.

[11] Y. Chen. *"Laser-Induced Gas Breakdown and Ignition"*. Ph.D. Dissertation. University of Tennessee, Knoxville, 1998.

[12] R. M. Gilgenbach, C. H. Ching, J. S. Lash, and R. A. Lindley. "Laser diagnostic experiments on KrF laser ablation plasma-plume dynamics relevant to manufacturing applications". *Phys. Plasmas*, 1:1619–1625, 1994.

[13] J. S. Lash, R. M. Gilgenbach, and C. H. Ching. "Laser-ablation-assisted-plasma discharges of aluminum in a transverse-magnetic field". *Appl. Phys. Lett.*, 65:531–533, 1994.

[14] Wolfgang Kautek, Jörg Krüger, M. Lenzner, S. Sartina, C. Spielmann, and F. Krausz. "Laser ablation of dielectrics with pulse durations between 20 fs and 3 ps". *Appl. Phys. Lett.*, 69:3146–3148, 1996.

[15] N. Wright. Verbal communications and technical assistance.

[16] EAI QUAD. QUAD 1100A Operation manual.

[17] EG&G Princeton Applied Research. Model 1303 Gate Pulse Interface Operating and Service Manual.

[18] EG&G Princeton Applied Research. Model 1304 Pulse Amplifier Operating and Service Manual.

[19] D. H. Plemmons. *"Electron density and temperature determination of a laser-induced plasma in hydrogen gas"*. M.S. Thesis. University of Tennessee, Knoxville, 1994.

[20] J. O. Hornkohl, C. Parigger, and J. W. L. Lewis. "On the use of line strengths in applied diatomic spectroscopy". Submitted to Optical Society of America for presentation in the 1995 conference on Laser Applications to Chemical and Environmental Analysis, March 1996.

[21] J. A. Coxon and S. Naxakis. "Rotational Analysis of the $B^2\Sigma^+ \longrightarrow X^2\Sigma^+$ System of the Aluminum Monoxide Radical, AlO". *J. Molec. Spectrosc.*, 30:102–113, 1985.

[22] H. Partridge, S. R. Langhoff, B. H. Lengsfield III, and B. Liu. "Theoretical Study of the AlO Blue-Green ($B^2\Sigma^+$–$X^2\Sigma^+$) Band System". *J. Quant. Spectrosc. Radiat. Transfer*, 30:449–462, 1983.

[23] M D Sakena, G S Ghodgaonkar, and M Singh. "The $B^2\ \Sigma^+$-$X^2\Sigma^+$ system of AlO". *J. Phys. B*, 22:1993–1996, 1989.

[24] J. Tellinghuisen. "Fast, accurate RKR computations". *J. Molec. Spectrosc.*, 44:194–196, 1972.

[25] R. N. Zare, A. L. Schmeltekopf, W. J. Harrop, and D. Albritton. "A direct approach for the reduction of diatomic spectra to molecular constants for the construction of RKR potentials". *J. Mol. Spectrosc.*, 46:37–66, 1973.

[26] W. H. Press, S. A. Teukolsky, W. T. Vetterling, and B. P. Flannery. *"Numerical Recipes in FORTRAN"*. Cambridge University Press, New York, 1992.

[27] J. O. Hornkohl, C. Parigger, and J. W. L. Lewis. "Temperature measurements from CN spectra in a laser-induced plasma". *J. Quant. Spectrosc. Radiat. Transfer*, 46:405–411, 1991.

[28] Coors Ceramics. http://www.coorsceramics.com/matprtab.htm.

Vita

Ivan G. Dors was born on 16 October 1974 in Manchester, NH. He grew up in Bow, NH and graduated from Bishop Brady High School in June of 1992. In the fall of 1996 he entered the University of New Hampshire (UNH). Starting in his sophomore year he worked part time as a laboratory assistant at the Space Science Group of the UNH Institute for the Study of Earth, Oceans, and Space. During his tenor with the Space Science Group he contributed to the development of energetic particle analyzers for the ACE and Cluster satellites. In May of 1996, he completed his bachelor of science degree with a major in physics, university honors in physics, and a minor in applied mathematics. The following August he accepted a research assistantship at the University of Tennessee Space Institute Center for Laser Applications where he earned a master of science degree in physics in May of 1998. Currently, he is working toward a Ph.D. in physics at UTSI.

Appendix

Appendix

Physical Properties of the Alumina Sample

Table A shows the physical properties of the 99.5% alumina target used in the investigations. This table is compiled from information provided by Coors Ceramics [28].

Table A: Physical properties of the alumina target.

Property	Test	Value	Units
Density	ASTM C20	3.8	g/cc
Color		White	
Water Absorption	ASTM C373	0	%
Elastic Modulus	ASTM C848	350	GPa
Poisson's Ratio	ASTM C848	0.22	
Flexural Strength	ASTM F417	375	MPa
Compressive Strength	ASTM C773	2500	MPa
Fracture Toughness Range	Notched Beam	4-5	MPa*m1/2
Hardness	Rockwell 45 N	82	GPa
Hardness	Knoop 1000g	13.7	GPa
Thermal Conductivity	ASTM C408	27.5	W/mK
CTE 25-1000	ASTM C372	8.2	10^{-6}/°C
Specific Heat	ASTM E1269	880	J/kg-K
Thermal Shock	H_2O Quench	200	ΔT_c
Dielectric Strength	ASTM D116	8.7	ac-kv/mm
Dielectric Loss	ASTM D2520	0.0002	25°C @ 1MHz
Volume Resistivity @ 298 K	ASTM D1829	$>10^{14}$	25°C Ω-cm
Volume Resistivity @ 1071 K	ASTM D1829	$>2x10^{10}$	500°CΩ-cm
Volume Resistivity @ 1298 K	ASTM D1829	$>2x10^{06}$	1000°CΩ-cm